# Buoyancy-induced flow and heat transfer in compressor rotors

Article (Accepted Version)

# BUOYANCY-INDUCED FLOW AND HEAT TRANSFER IN COMPRESSOR ROTORS

**Hui Tang**

Department of Mechanical Engineering, University of Bath

Bath, BA2 7AY, United Kingdom

h.tang2@bath.ac.uk

**Mark R Puttock-Brown**

Thermo-Fluid Mechanics Research Centre

School of Engineering and Informatics, University of Sussex

Farlmer, Brighton, BN1 9RH, United Kingdom

M.Puttock@sussex.ac.uk

**J Michael Owen**

Department of Mechanical Engineering, University of Bath

Bath, BA2 7AY, United Kingdom

ensjmo@bath.ac.uk



## ABSTRACT

The buoyancy-induced flow and heat transfer inside the compressor rotors of gas-turbine engines affects the stresses and radial growth of the compressor discs, and it also causes a temperature rise in the axial throughflow of cooling air through the centre of the discs. In turn, the radial growth of the discs affects the radial clearance between the rotating compressor blades and the surrounding stationary casing. The calculation of this clearance is extremely important, particularly in aeroengines where the increase in pressure ratios results in a decrease in the size of the blades.

In this paper, a published theoretical model - based on buoyancy-induced laminar Ekman-layer flow on the rotating discs - is extended to include laminar free convection from the compressor shroud and forced convection between the bore of the discs and the axial throughflow. The predicted heat transfer from these three surfaces is then used to calculate the temperature rise of the throughflow. The predicted temperatures and Nusselt numbers are compared with measurements made in a multi-cavity compressor rig, and mainly good agreement is achieved for a range of Rossby, Reynolds and Grashof numbers representative of those found in aeroengine compressors. Owing to compressibility effects in the fluid core between the discs – and as previously predicted -

increasing rotational speed can result in an increase in the core temperature and a consequent decrease in the Nusselt numbers from the discs and shroud.

## 1 INTRODUCTION

Fig. 1 shows a high-pressure (HP) compressor rotor where cooling air flows axially through the clearance between the bores of the compressor discs and a central shaft, which usually rotates at a speed different from that of the discs. (In some compressors, there can also be a radial inflow of air and the throughflow can be in the opposite direction to that shown; this case is not considered in this paper.)

In the quest for ever higher pressure ratios - which can exceed 50:1 in modern aeroengines - the size of the compressor blades decrease as the pressure ratio increases. Consequently the clearance between the blades and the casing becomes increasingly important: too large a clearance reduces the compressor efficiency; too small a clearance can be catastrophic. As well as affecting the stresses and the blade clearances, the heat transfer from the discs and shrouds creates a rise in the temperature of the axial throughflow of cooling air. As this air is used for cooling downstream turbine components, the designer needs to calculate the temperature of the throughflow as it passes through the centre of the compressor rotor.

Recently, a simplified model [2], which is both fast and accurate, has been developed to predict the disc temperatures for buoyancy-induced flow in open cavities with an axial throughflow of cooling air. The model was validated using the measurements of disc temperatures in a multi-cavity compressor rig [3]. The authors have also developed a separate model for closed cavities [4] which are sealed at their centres, like those found in some industrial gas turbines.

In this paper, the two buoyancy models [2, 4] are combined to calculate heat transfer from the discs and shroud in an open cavity, and an empirical correlation is used to estimate the heat transfer from the bore of the cobs to the throughflow. Knowing the total heat transfer from all these rotating surfaces, it is then possible to calculate the temperature rise of the throughflow, and the predictions of Nusselt numbers and temperatures are compared with measurements made in in a multi-cavity compressor rig.

As far as the authors are aware, this is the first time that the combined heat transfer from the discs and shroud and the temperature rise of the cooling air have been calculated. A brief review of relevant research is given in Section 2, and the theoretical models and the experimental rig are described in Sections 3 and 4. Predictions and measurements are compared in Section 5, and Section 6 includes a summary of the conclusions.

## 2 REVIEW OF RELEVANT RESEARCH

Fig. 2 shows a simplified diagram of a single cavity, where the shroud is the cylindrical casing at the outer radius of the discs and the cobs are the bulbous hubs at the centre of the discs. As a comprehensive review of buoyancy-induced flow in rotating cavities is given in [5], only those papers of direct relevance to the work discussed below are included here. For more extensive coverage of rotating flows in general the reader is referred to [6].

The modelled disc temperatures and Nusselt numbers, using the equations in [2, 3]( also see Section 3), were compared with the measured disc temperatures and the experimentally-derived Nusselt numbers for the 19 test cases of Atkins and Kanjirakkad [7] over a wide range of parameters. The experimentally-derived Nusselt numbers were obtained from the measured disc temperatures using the Bayesian model described in [8]. The mainly good agreement between theory and experiment provided evidence that the flow is indeed laminar, even at Grashof numbers of order those found in compressors. The authors attributed the laminar flow to the large Coriolis forces in the cavity, which tend to damp out turbulence, and to the fact that the relative speed between the core and the discs was very small.

Buoyancy-induced flow in a *closed* rotating cavity with a hot outer cylindrical surface and a cold inner one was modelled by Tang and Owen [4] by assuming that, as for the discs, the heat transfer is caused by laminar free convection. The predictions were validated using the measured Nusselt numbers of Bohn et al. [9], which were obtained in three different cavities and for a range of pressures between 1 and 4 bar and Grashof numbers up to $10^{12}$.

Long and Childs [10] measured the variation of the shroud Nusselt numbers with Grashof numbers in a multi-cavity compressor rig similar to the one described in Section 4. Although the data were bounded by empirical correlations based on laminar and turbulent free convection for a horizontal heated plate, the Grossman and Lohse [11] equation for Rayleigh-Bénard convection between parallel plates provided the best agreement with the data.

## 3 THEORETICAL MODELS

Three of the four models described below provide equations to calculate the heat transfer from the discs and the shroud to the core and from the cob to the axial throughflow; the fourth model uses these equations to calculate the temperature rise of the throughflow.

### 3.1 Heat transfer from disc to core

#### *3.1.1 Modelled Nusselt numbers*

The term *modelled Nusselt numbers* is used here to refer to the values that were determined using the equations given below, which are based on the Ekman-layer model in [2]. The Nusselt number for the discs is given by

$$Nu_c = \frac{1}{2}\frac{x_a^{1/2}}{I^{1/4}} Gr_c^{1/4} \left[ (\theta - Co) \left( \frac{\rho_c}{\rho_{c,b}} \right)^2 x^5 \right]^{1/3} \tag{3.1}$$

where *Co*, the Coriolis parameter, the integral *I* and the density ratio are given below.

$$Co = 2(1 - \frac{\Omega_c}{\Omega}) \frac{1}{\beta(T_{o,b} - T_{c,b})} \tag{3.2a}$$

$$I = \int_{x_a}^{1} x^{11/3} \left[ (\theta - Co) \left( \frac{\rho_c}{\rho_{c,b}} \right)^2 \right]^{1/3} dx \tag{3.2b}$$

$$\frac{\rho_c}{\rho_{c,a}} = \left[ 1 + \frac{\gamma - 1}{2} Ma_c^2 (x^2 - x_a^2) \right]^{1/(\gamma - 1)} \tag{3.2c}$$

The other symbols are defined in the Nomenclature, and further details are given in [2].

### *3.1.2 Modelled disc temperatures*

This is a conjugate problem: the Nusselt numbers depend on the disc temperature, which in turn depends on the Nusselt numbers. In [3], eq (3.1) was solved in conjunction with the numerical solution of the general fin equation for the disc, which is given by

$$\frac{d^2 T_o}{dr^2} + \left( \frac{1}{r} - \frac{2}{t} \frac{cos\alpha}{sin\alpha} + \frac{1}{k_s} \frac{dk_s}{dT_o} \frac{dT_o}{dr} \right) \frac{dT_o}{dr} - \frac{2h_f}{k_s t sin\alpha} \left( T_o - T_f \right) = 0 \tag{3.3}$$

The geometry of the disc, which is shown in Fig. 3, is based on the experimental Sussex rig described in Section 4, and the thermal conductivity, $k_s$, of the titanium disc is given in [3]. The finite-difference equations used for the numerical solution of eq (3.3) are also given in [3]. At $r = b$, the measured value of $T_{o,b}$ was used as the boundary condition. At $r = a$, a convective boundary condition based on the heat transfer coefficient for the inner surface of the cob, as discussed in Section 3.3, was used. (In [3], the measured temperature at the outer edge of the cob, at $r = a'$ in Fig. 4, was used as the boundary condition for the inner surface of the disc, and the theoretical temperature of the cob was not calculated.)

The coupled eqs (3.1) and (3.3) were solved iteratively to calculate the theoretical Nusselt numbers and disc temperatures. To compare with the experimentally-derived values in section 3.1.3, the non-dimensional disc temperatures, Θ (eq 3.4), and Nusselt numbers, $Nu_f$ (eq 3.5) were used.

$$\Theta = \frac{T_o - T_f}{T_{o,b} - T_f} \tag{3.4}$$

$$Nu_f = \frac{h_f r}{k_f} \tag{3.5}$$

As discussed in Section 3.4, the disc Nusselt numbers were used in the calculation of the theoretical temperature rise of the throughflow

#### *3.1.3 Experimentally-derived Nusselt numbers and disc temperatures*

The general fin equation, eq (3.3), was solved numerically - in conjunction with the measured disc temperatures, using the Bayesian statistical model described in [8] - to calculate what are referred to here as the *experimentally-derived* Nusselt numbers and disc temperatures. The Nusselt numbers and the 95% confidence interval were determined from the *inverse solution* of eq (3.3) (where the temperature distribution was specified); the disc temperatures were determined from the *direct solution* (where the Nusselt numbers were specified).

The temperatures of both surfaces of the instrumented disc were measured in the experiments; for the inverse solution of eq (3.3), the mean of the two sets of measured temperatures was used. (Apart from those on the cob surfaces, the differences between the two sets of temperature were smaller than the uncertainty in the measured values.)

The experimentally-derived values are compared with the theoretical values in Section 5.

### 3.2 Heat transfer from shroud to core

As assumed in [4], the heat transfer from the rotating shroud to the core was calculated by adapting a standard correlation for laminar free convection from a horizontal plate in a gravitational field [12], where the length-scale is based on the area: perimeter ratio of the plate for a shroud. For the rotating shroud, this ratio equals $s/2$, where $s$ is the axial width of the shroud, and the gravitational acceleration for the plate is replaced by the centripetal acceleration at $r = b$.

To compare the theoretical predictions with the experimental measurements, the temperature of the shroud, $T_{sh}$, was assumed to equal $T_{o,b}$ , the measured disc temperature at $r = b$, and the air temperature in the core close to the shroud, $T_{c,b}$ , was calculated using the compressibility equations in [2] for $x = 1$. Consequently

$$Nu_{sh} = C(Gr_{sh}Pr)^{0.25} \tag{3.6}$$

where $C$ is an empirical constant, and the definitions of $Nu_{sh}$ and $Gr_{sh}$ are

$$Nu_{sh} = \frac{h_{sh}(s/2)}{k_{c,b}} = \frac{q_{sh}(s/2)}{k_{c,b}(T_{sh} - T_{c,b})} \tag{3.7}$$

and

$$Gr_{sh} = \frac{\rho_{c,b}^2 \Omega_c^2 b}{\mu_{c,b}^2} \frac{T_{sh} - T_{c,b}}{T_{c,b}} \left(\frac{s}{2}\right)^3 \tag{3.8}$$

The theoretical heat flux from the shroud can then be computed by

$$q_{sh} = 2Nu_{sh} k_{c,b} \left(T_{sh} - T_{c,b}\right)/s \tag{3.9}$$

and

$$\dot{Q}_{sh} = 2\pi b s q_{sh} = 4\pi b k_{c,b} Nu_{sh} (T_{o,b} - T_{c,b}) \tag{3.10}$$

For horizontal plates, the appropriate value of $C$ is 0.54. In [4], for the case of the shrouds in closed rotating cavities (with insulated discs), a value of $C = 0.32$ was used to fit all the experimental data for three different cavities over a wide range of Grashof numbers. For the open cavity in the compressor rig, a constant, 0.44, was chosen to obtain the best agreement with the experiments.

### 3.3 Heat transfer from cob to axial throughflow

The heat transfer from the cob to the throughflow is assumed to be by *forced* convection. It is expected that the Nusselt number will depend on the rotational speed of the inner bore of the cob and on the axial velocity of the throughflow. It will also depend on the cob geometry and on the condition of the upstream flow, which in turn will depend on the flow in the upstream cavities. With the limited data available, it is not possible to consider all these effects, and for simplicity it is assumed here that the heat transfer depends on the resultant velocity, *U*, where

$$U = \sqrt{W^2 + (\Omega a)^2} \tag{3.11}$$

and *W* is the bulk-mean axial velocity of the throughflow. It is also assumed that

$$Nu_{cob} = A Re_T^B \tag{3.12}$$

where

$$Nu_{cob} = \frac{q_{cob} l}{k_f (T_{cob} - T_f)} \tag{3.13}$$

and

$$Re_T = \rho_f U l / \mu_f \tag{3.14}$$

*A* and *B* are empirical constants, and *l* is the axial length of the cob.

The fin equation, eq (3.3), was solved using eq (3.12) to provide the convective boundary condition at $r = a$; $T_{cob}$ in eq (3.13) was assumed to equal $T_{o,a}$, the value of $T_o$ calculated at $r = a$. Using iterative solutions of the equations, values of $A = 0.69$ and $B = 0.37$ were found to give the best agreement between the theoretical and experimental disc temperatures. So eq (3.12) becomes

$$Nu_{cob} = 0.69{Re_T}^{0.37} \tag{3.15}$$

The heat flow from the inner surface of the cob to the throughflow was calculated from

$$\dot{Q}_{cob} = 2\pi a l q_{cob} \tag{3.16}$$

where $q_{cob}$ was calculated from eq (3.13).

It is shown in Section 5 that – for the range of the experiments in this paper - the calculated heat loss from the cobs was very small, compared with that from the discs and shroud, and that the predictions were relatively insensitive to the magnitude of $Nu_{cob}$. Although other empirical correlations could be used instead of eq (3.15), their overall effect on the predicted temperatures is expected to be negligible.

### 3.4 Temperature rise of axial throughflow

The heat transferred indirectly from the discs and shroud to the core, together with the heat transferred directly from the cob bore, all contribute to the temperature rise of the throughflow. The temperature difference across a shear layer would create the heat flow from the core to the throughflow.

Referring to the control volume shown in Fig. 4, for disc i, it is assumed that $\dot{Q}_{u,i} \approx \dot{Q}_{d,i}$. (In engines, it is probable that $\dot{Q}_{u,i} < \dot{Q}_{d,i}$, but allowing for this is beyond the scope of the current version of the model.) The heat transfer from one face of the disc shown in Fig.4 can be calculated from

$$\dot{Q}_u = \dot{Q}_d = 2\pi \int_a^b k_f Nu_f (T_o - T_f)/\sin\alpha \, dr \tag{3.17}$$

It is also assumed that, as the rotational speed of the core is very close to that of the discs, the work term is significantly smaller than the heat transfer terms. If $\dot{m}_f$ is the mass flow rate of the throughflow, then an energy balance for the control volume shows that

$$\Delta T_f = \frac{2\dot{Q}_{u,i} + \dot{Q}_{sh,i} + \dot{Q}_{cob,i}}{c_p \dot{m}_f} \tag{3.18}$$

where $\Delta T_f = T_{f,i+1/2} - T_{f,i-1/2}$. The values of $\dot{Q}_{sh,i}$, $\dot{Q}_{cob,i}$can be calculated using the equations given in Sections 3.2 and 3.3, and the theoretical values of $\Delta T_f$ are compared with the experimental values in Section 5.

## 4 EXPERIMENTAL FACILITY

### 4.1 Experimental rig

The experimental apparatus is shown in Fig. 5 along with the instrumentation relevant to this paper. Full rig details are reported in [13], so only a brief summary is presented here.

The rotor disc pack was formed of five titanium discs that form four cylindrical cavities, all having an outer shroud diameter of 491.3 mm, supported by two bearings. The first three cavities (in the direction of flow)

had an inner radius of $a = 70.1mm$, an axial gap of $s = 42.9\ mm$ and an outer radius $b = 220\ mm$, giving a gap ratio of $G = 0.195$. The rotor was bolted together at the periphery using 16x10 mm titanium rods with threaded ends and aerospace grade nuts, and continuous silicone O-rings were used between each disc. Following a previous build, the radial-inflow paths described by Atkins [14] were plugged to stop air from escaping via the holes in the cavity outer radii. The heat transfer from the compressor main-stream air was simulated using a 24 kW array of radiant heaters fixed to the outer casing. The disc pack was driven by a 22 kW electric motor, which allowed a maximum speed of 8000 rpm. The new central mild-steel shaft, which was driven by a 3kW electric motor, had an outer radius $r_s = 52\ mm$, giving a hydraulic diameter $d_h = 36.2\ mm$. The shaft could be co-rotated or counter-rotated with a speed relative to the rotor of 16,000 rpm.

The throughflow air was supplied via 2 x 30 mm pipes, which fed the air in the circumferential direction into an annular plenum, transferring radially inwards through 12 x 24 mm holes though the inner radius of the plenum and the outer radius of the shaft-assembly mount. The air was then turned 90° to the axial direction, flowing through an annular duct formed by the central shaft and the rotor stub-shaft; a convergence in the duct formed an annular space equal to that in rotor test-section. Finally there were 6 x 10 mm-wide rectangular blocks bolted to the rotor stub-shaft forming a similar flow restriction to the circumferential array of 6 x 25 mm holes in the rotor endplate, where the flow exited the test section. There was no diffuser plate.

The throughflow air, which was supplied by an Atlas Copco ZT250 compressor, was immediately ducted to an Atlas Copco air dryer which removed any moisture. The air flow rate, which was measured using an on-site-calibrated Venturi, was controlled via three stages. Initially a manual ball-valve was used to open the main supply line, then a remote bypass-valve was gradually closed to increase the supply to the rig. Finally, a butterfly-valve, located downstream of the rig exhaust, was used to pressurise the rig to approximately 1.2 bar, allowing the pressure-balanced labyrinth seals to maintain a differential pressure of ±10 mbar with negligible leakage.

### 4.2 Instrumentation

The temperatures of the rotor surface were measured using glass-fibre-insulated K-type thermocouples with a wire diameter of 0.25 mm. The junction was formed by electro-welding the two wires, all taken from the same batch, in an Argon gas atmosphere, and the nominal diameter of the beads was 0.4 mm. The beads were peened into a shallow slot in the surface using a centre-punch to give a cold-welded metal-to-metal contact. This process left a shallow depression in the surface, which was filled with an epoxy resin and finished to give an aerodynamically-smooth surface. The thermal-disturbance errors were further reduced by leading the thermocouple wires along tangential slots for at least 10 wire-diameters before they were led out radially to the

instrumentation holes in the rotor periphery. The thermal disturbance errors due to the embedding process have been studied in previous programmes and found to give errors of the order 0.1 K. A Datatel radio-telemetry system, with on-board cold-junction compensation and a recording frequency of 3Hz, was used to transmit the thermocouple signals to the data-logging system.

The central shaft contained 36 thermocouples giving both surface and air measurements at nine axial locations. The surface thermocouples were installed in a similar fashion to those in the rotor, and the unsupported air thermocouples protruded 4 mm from the shaft surface. Figure 5 shows the location of the air thermocouples used in this paper. They were located in the mid-plane of both the upstream and downstream cavities and the mid-plane of the disc. The measurements were recorded by a second Datatel radio-telemetry system, again with on-board cold-junction compensation, and in both cases the magnitude of the total uncertainty was estimated to be no greater than 0.5K.

## 5 COMPARISON BETWEEN THEORETICAL AND EXPERIMENTAL VALUES

Table 1 shows the principal experimental parameters, the approximate ranges of which were: $4.1 \times 10^{11} < Gr_f < 10^{12}, 0.15 < \beta\Delta T < 0.35, 1.6 \times 10^6 < Re_\phi < 3.0 \times 10^6, 1.1 \times 10^5 < Re_z < 5.1 \times 10^5$ and $0.1 < Ro < 0.6$. As the inner shaft could be held stationary or independently rotated to achieve co-rotation or contra-rotation, the ratios of shaft: disc rotational speeds are also shown.

### 5.1 Disc temperatures and Nusselt numbers

The calculation of the theoretical temperatures and Nusselt numbers for the discs and the experimentally-derived values is described in Section 3.1. The Coriolis parameter defined by eq (3.2f) was chosen to minimise the difference between the theoretical and experimental average disc temperatures, $\Theta_{av,th}$ and $\Theta_{av,exp}$ respectively, where

$$\Theta_{av} = \frac{2\int_{x_a}^{1} \Theta x dx}{1 - x_a^2} \tag{5.1}$$

As shown in Fig.6, a value of $Co = 0.030$ provides a good fit, with a standard deviation of 0.014, and the individual values of $\Theta_{av,th}$ and $\Theta_{av,exp}$ are included in Table 1. (It was shown in [3] that the theoretical Nusselt numbers were relatively insensitive to the value of $Co$. In that paper, the Rossby numbers tended to be higher and their range ($0.3 < Ro < 5$) larger than for the experiments described here; a value of $Co = 0.07$ was found to give the best fit to the data. It is possible that *Co* may increase as *Ro* increases, but more evidence is required to support that conjecture.)

Figs 7 to 10, corresponding to Ro ≈ 0.6, 0.3, 0.2 and 0.1 respectively, show the comparison between the modelled and experimentally-derived nondimensional disc temperatures and Nusselt numbers. As stated in Section 3.1, the experimentally-derived Nusselt numbers were computed from the measured disc temperatures using a Bayesian statistical model [8], and the shading shows the 95% uncertainty in $Nu_f$.

As in [3], and consistent with the experimental evidence, the modelled Nusselt numbers were assumed to be zero at the inner radius of the disc and, as stated above, a value of *Co* = 0.030 was used for the Coriolis parameter in all 10 cases. *It should be noted that - unlike in [3] - the results shown here include the modelled Nusselt numbers and temperatures for the cob.* An over-prediction of $Nu_f$ tends to result in an under-prediction of the disc temperature, and vice versa, but in the main there is good agreement between the modelled and experimental results. It should also be noted that the relative speed of the inner shaft (see Table 1) appears to have had no significant effect on the results. (This was also observed in [10] for heat transfer measurements on the shroud in a multi-cavity compressor rig.)

Comparison between Figs 7 and 9a shows the effect of compressibility on the Nusselt numbers. In Fig. 9a, the Grashof number is higher but the maximum value of the Nusselt number is much lower than it is in Fig.7. The reduction in $Nu_f$ despite the increase in $Gr_f$ is caused by the fact that $Re_\phi$ in Fig.9a is higher (and therefore the rise in core temperature is also higher) than that in Fig. 7; this phenomenon was also observed in [3].

**5.2 Temperature rise of axial throughflow**

The method used to predict $\Delta T_f$, the bulk-mean total-temperature rise of the axial throughflow, was described in Section 3.4. For convenience, eq (3.17) is repeated below removing the subscript *i* and adding *th* to denote the theoretical or modelled value of $\Delta T_f$.

$$\Delta T_{f,th} = \frac{2\dot{Q}_u + \dot{Q}_{sh} + \dot{Q}_{cob}}{c_p \dot{m}_f} \tag{5.2}$$

Knowing the radial distribution of the disc temperatures and the Nusselt numbers, $\dot{Q}_u$, the heat transfer from the upstream surface of the disc, can be calculated by integrating the heat flux from $r = a$ to $r = b$. Knowing the value of $T_{c,b}$, the modelled core temperature at $r = b$, $\dot{Q}_{sh}$, the heat transfer from the shroud, can be calculated using eqs (3.6) to (3.10). Knowing the value of $T_{o,a}$, $\dot{Q}_{cob}$, the heat transfer from the cob, can be calculated using eqs (3.11) to (3.16).

Fig. 11 shows the comparison between the modelled and experimental values of $\Delta\Theta_f$ where

$$\Delta\Theta_f = \frac{\Delta T_f}{T_{o,b} - T_f} \tag{5.3}$$

The modelled values were calculated using a value of $C = 0.44$ in eq (3.5) for the shroud heat transfer. This value, which was chosen to minimise the least-squares error between the modelled and experimental values, is intermediate between 0.54 for laminar free convection from a horizontal plate [12] and 0.32 for the shrouds in closed rotating cavities [4]. (The correlation of Long and Childs [10] produced significant overestimates of the temperature rise.) The predicted relative contributions of heat transfer from the shroud, both disc surfaces and the cob bores to the rise in throughflow temperature were approximately 62%, 37% and 1% respectively for the range of conditions tested.

It is important to emphasise that the empirical correlation for the cob Nusselt number given by eq (3.14) may not be valid outside the range of experiments reported in this paper. The values of $Nu_{cob}$ used here were between 42 and 52, and an average value of 48 gave predictions similar to the ones discussed. As the relative effect of the heat transfer from the cob bore has only a very small effect on the temperature rise of the throughflow, and as the results are only weakly affected by the precise value of $Nu_{cob}$, it is unlikely that other correlations would make a significant difference to the predictions.

## 6 CONCLUSIONS

A previously published laminar model of buoyancy-induced flow [2], which predicts the Nusselt numbers and temperatures of the rotating discs inside compressor rotors, has been extended to calculate the heat transfer from the shrouds and from the cobs and to calculate the temperature rise of the axial throughflow. The modelled results have been compared with temperature measurements made in a multi-cavity compressor rig for a range of Rossby, Reynolds and Grashof numbers representative of those found in aeroengines. The predictions of Nusselt numbers and disc temperatures have also been compared with experimentally-derived values obtained by applying a Bayesian model [8] to the measured temperatures.

A value of $Co = 0.030$ for the Coriolis parameter was found to provide a mainly good fit between the modelled and experimentally-derived disc temperatures and Nusselt numbers even at Grashof numbers up to $10^{12}$. (It should be noted that, unlike [3] where the temperatures of inner and outer radii of the disc was specified as a boundary conditions, in the current version of the model the temperature and Nusselt numbers for the entire disc require only the temperatures of the outer radius of the disc and the axial throughflow to be given.) As found in [2], compressibility effects in the core can result in a *reduction* of the disc Nusselt numbers with increasing Grashof numbers. No significant effect of the relative rotational speed of the inner shaft was observed.

As in [4], the model for the shroud heat transfer used a correlation for laminar free convection from a horizontal plate, with the gravitational acceleration replaced by centripetal acceleration for the rotating shroud. A

value of $C$ = 0.44 for the single empirical constant in the correlation was chosen to give the best predictions of the measured temperature rise of the throughflow. This value of $C$ is intermediate between 0.54, the value for horizontal plates, and 0.32, the value used in [4] for the shrouds in closed rotating cavities. The authors consider that the value of $C$ for the open cavity will tend to that for the closed cavity as the axial clearance between the cobs is reduced, but more experimental evidence is required to test that hypothesis.

The heat transfer between the bore of the cobs and the throughflow was assumed to be by forced convection. An empirical correlation was assumed for the cob Nusselt number, and two empirical constants were chosen to provide the best fit between the measured and predicted disc temperatures. The relative heat transfer from the cob to the throughflow was small, and so the predicted temperature rise of the throughflow was relatively insensitive to the magnitude of the cob Nusselt numbers.

The modelled values of the heat flow from the shroud, discs and cob were used to predict the temperature rise of the throughflow, and good agreement was achieved between the predicted and measured values. The average contributions from the shroud, both disc surfaces and the cob bores to the temperature rise were predicted to be approximately 62%, 37% and 1% respectively for the range of conditions tested.

The fact that laminar buoyancy models can be used for large Grashof numbers, where most engineers would expect the flow to be turbulent, is attributed to the large Coriolis accelerations in the fluid core and to the fact that there is only a small difference between the rotational speed of the core and that of the discs.

The model described above assumes that both discs are at the same temperature, whereas in engines the downstream disc will usually be hotter than the upstream one. There are plans for future experiments, both steady-state and transient, in a new compressor rig in which the discs can be differentially heated and the cob geometry can be changed.

## Nomenclature

| | |
|---|---|
| $a$ | inner radius |
| $a'$ | inner radius of outer edge of the cob |
| $A, B$ | empirical constants |
| $b$ | outer radius |
| $c$ | speed of sound in core ($= \sqrt{\gamma R T_{c,a}}$) |
| $c_p$ | specific heat capacity at constant pressure |
| $C$ | empirical constant |
| $d_h$ | hydraulic diameter ($= 2(a - r_s)$) |

| | |
|---|---|
| $Co$ | Coriolis parameter (see eq.3.2a) |
| $G$ | gap ratio ($= s/b$) |
| $Gr$ | Grashof number |
| $Gr_c$ | Grashof number in theory ($= Re_\phi'^2 \beta(T_{o,b} - T_{c,b})$) |
| $Gr_f$ | Grashof number in experiments ($= (1 - a/b)^3 Re_\phi^2 \beta(T_{o,b} - T_f)$) |
| $Gr_{sh}$ | shroud Grashof number ($= (s/2b)^3\ Re_\phi^2 \beta(T_{sh} - T_{c,b})$) |
| $h$ | heat transfer coefficient |
| $h_c$ | heat transfer coefficient based on $T_c$ ($= q_o/(T_o - T_c)$) |
| $h_f$ | heat transfer coefficient based on $T_f$ ($= q_o/(T_o - T_f)$) |
| $h_{sh}$ | shroud heat transfer coefficient ($q_{sh}/(T_{sh} - T_{c,b})$) |
| $i$ | disc number |
| $I$ | integral (see eq. 3.2b) |
| $k$ | thermal conductivity of air |
| $k_s$ | thermal conductivity of disc |
| $l$ | axial length of cob |
| $\dot{m}_f$ | mass flow rate of axial throughflow (kg/s) |
| $Ma_c$ | Mach number in core ($= \Omega_c b/c$) |
| $Nu$ | local Nusselt number |
| $Nu_c$ | Nusselt number based on $h_c$ ($= h_c r/k_{c,b}$) |
| $Nu_{cob}$ | cob Nusselt number ($= q_{cob} l/(T_{o,a} - T_f)k_f$) |
| $Nu_f$ | Nusselt number based on $h_f$ ($= h_f r/k_f$) |
| $Nu_{sh}$ | shroud Nusselt number ($= q_{sh}(s/2)/(T_{sh} - T_{c,b})k_{c,b}$) |
| $Pr$ | Prandtl number |
| $q_{cob}$ | heat flux from cob to air |
| $q_o$ | heat flux from disc to air |
| $q_{sh}$ | heat flux from shroud to air |
| $\dot{Q}$ | heat flow rate |
| $r$ | radius |
| $r_s$ | radius of inner shaft |

| | |
|---|---|
| $R$ | gas constant |
| $Re_T$ | Reynolds number for cob ($= \rho_f U l/\mu_f$) |
| $Re_z$ | axial Reynolds number ($= \rho_f W d_h/\mu_f$ ) |
| $Re_\phi$ | rotational Reynolds number based on $\rho_f$ ($= \rho_f \Omega b^2/\mu_f$) |
| $Re_\phi'$ | rotational Reynolds number based on $\rho_{c,b}$ ($= \rho_{c,b} \Omega b^2/\mu_{c,b}$) |
| $Ro$ | Rossby number ($= W/\Omega a$) |
| $s$ | axial space between discs in cavity |
| $t$ | disc thickness |
| $T$ | static temperature |
| $T_c, T_f, T_o, T_{sh}$ | temperature of core, throughflow, disc, shroud |
| $U$ | resultant velocity ($= \sqrt{W^2 + (\Omega a)^2}$) |
| $W$ | axial component of velocity of throughflow |
| $x$ | nondimensional radius ($= r/b$ ) |
| $x_a$ | radius ratio ($= a/b$) |
| $\alpha$ | angle of gradient of disc surface |
| $\beta$ | volume expansion coefficient ($= 1/T_{ref}$) |
| $\gamma$ | ratio of specific heats |
| $\theta$ | nondimensional temperature ($= (T_o - T_c)/(T_{o,b} - T_{c,b})$) |
| $\Theta$ | nondimensional disc temperature ($= (T_o - T_f)/(T_{o,b} - T_f)$) |
| $\mu$ | dynamic viscosity |
| $\rho$ | density |
| $\Omega, \Omega_c$ | angular speed of disc, core |

*Subscripts*

| | |
|---|---|
| $a$ | value at $r = a$ |
| $av$ | radially-weighted average value |
| $b$ | value at $r = b$ |
| $c$ | value in core |
| $cob$ | value on cob |

| | |
|---|---|
| $d$ | value on downstream disc surface |
| $exp$ | experimental value |
| $f$ | value in axial throughflow |
| $i$ | values for the $i^{th}$ disc in a multi-cavity system |
| $o$ | value on disc surface |
| $ref$ | reference value |
| $sh$ | value on shroud |
| $th$ | theoretical or modelled value |
| $u$ | value on upstream disc surface |
| $\phi, r, z$ | circumferential, radial, axial direction |

## ACKNOWLEDGMENTS

We wish to thank the China Scholarship Council for supporting Hui Tang during her study for a PhD degree at the University of Bath.

## References

1. Long, C.A., Miché, N.D.D. and Childs, P.R.N, 2007, "Flow Measurements insided a Heated Multiple Rotating Cavity with Axial Throughflow," Int. J. Heat Fluid Flow, 28(06),1391-1404.
2. Owen, J.M. and Tang, H., 2015, "Theoretical Model of Buoyancy-Induced Flow in Rotating Cavities," ASME J. Turbomach, 137(11), 111005.
3. Tang, H. and Owen, J.M., 2017, "Effect of Buoyancy-Induced Rotating Flow on Temperature of Compressor Discs," ASME J. Eng. Gas Turbines Power, 139(06), 062506.
4. Tang, H. and Owen, J.M., 2017, "Theoretical Model of Buoyancy-Induced Heat Transfer in Closed Compressor Rotors," ASME J. Eng. Gas Turbines Power, to appear.
5. Owen, J. M. and Long, C. A., 2015, "Review of Buoyancy-Induced Flow in Rotating Cavities," ASME J. Turbomach, 137(11), 111001.
6. Childs, P. R.N., 2011, "Rotating flow", Elsevier, Oxford, UK.
7. Atkins, N.R. and Kanjirakkad V., 2014, "Flow in a Rotating Cavity With Axial Throughflow at Engine Representative Conditions," ASME Paper GT2014-27174.

8. Tang, H., Shardlow, T., and Owen, J.M., 2015, "Use of Fin Equation to Calculate Nusselt numbers for Rotating Discs," ASME J. Turbomach, 137(12), 121003.
9. Bohn, D., Deuker, E., Emunds, R. and Gorzelitz, V., 1995, "Experimental and Theoretical Investigations of Heat Transfer in Closed Gas-Filled Rotating Annuli," ASME J. Turbomach., 117(1), 175-183.
10. Long, C.A. and Childs, P.R.N., 2007, "Shroud Heat Transfer Measurements inside a Heated Multiple Rotating Cavity with Axial Throughflow," Int.J.Heat Fluid Flow, 28, pp 1405-1417.
11. Grossmann, S. and Lohse, D., 2000, "Scaling in Thermal Convection: a Unifying Theory," J. Fluid Mech., 407, pp.27-56.
12. Lloyd, J.R. and Moran, W.R., 1974, "Natural Convection Adjacent to Horizontal Surfaces of Various Planforms," ASME paper 74-WA/HT-66.
13. Puttock-Brown, M., 2017, "Experimental and Numerical Investigation of Flow Structure and Heat Transfer in Gas Turbine H.P. Compressor Secondary Air Systems", Thesis to be submitted for DPhil, University of Sussex.
14. Atkins, N. R., 2013, "Investigation of a Radial-Inflow Bleed as a Potential for Compressor Clearance Control," ASME Paper GT2013-95768.

| | *Ro* ≈ 0.6 | *Ro* ≈ 0.3 | | | | *Ro* ≈ 0.2 | | | | *Ro* ≈ 0.1 |
|---|---|---|---|---|---|---|---|---|---|---|
| *Case* | a | b1 | b2 | c1 | c2 | c3 | c4 | c5 | c6 | d |
| *Ro* | 0.61 | 0.31 | 0.31 | 0.16 | 0.16 | 0.18 | 0.17 | 0.17 | 0.17 | 0.10 |
| $Gr_f/10^{11}$ | 2.5 | 10 | 10 | 4.2 | 4.5 | 6.8 | 7.2 | 7.2 | 7.8 | 4.1 |
| $\beta\Delta T$ | 0.32 | 0.35 | 0.35 | 0.15 | 0.16 | 0.33 | 0.32 | 0.32 | 0.34 | 0.29 |
| $Re_\phi/10^6$ | 1.6 | 3.0 | 3.0 | 3.0 | 3.0 | 2.5 | 2.7 | 2.7 | 2.7 | 2.1 |
| $Re_z/10^4$ | 5.1 | 5.0 | 5.0 | 2.5 | 2.5 | 2.4 | 2.4 | 2.4 | 2.5 | 1.1 |
| $N_{shaft}/N_{disc}$ | 1.0 | 0.34 | 1.0 | 0.34 | -0.34 | 1.0 | 0.34 | -0.34 | 0 | 0 |
| $\Theta_{av,exp}$ | 0.35 | 0.35 | 0.33 | 0.50 | 0.49 | 0.36 | 0.38 | 0.39 | 0.37 | 0.41 |
| $\Theta_{av,th}$ | 0.37 | 0.35 | 0.35 | 0.50 | 0.49 | 0.37 | 0.37 | 0.37 | 0.36 | 0.40 |

**Table 1: Experimental parameters**

Journal of Engineering for Gas Turbines and Power. Received June 07, 2017;
Accepted manuscript posted December 15, 2017. doi:10.1115/1.4038756


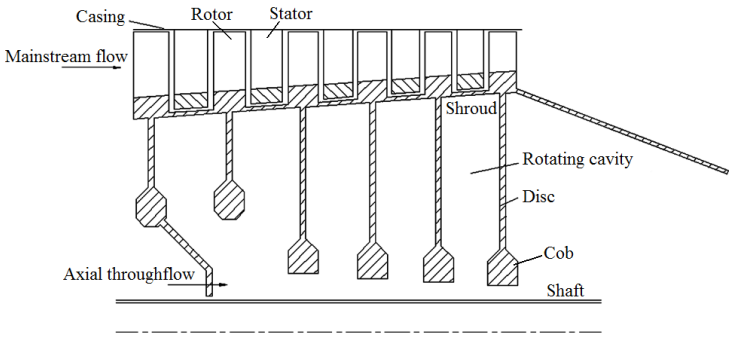


**Fig. 1: Schematic diagram of gas turbine high-pressure compressor rotor [1]**

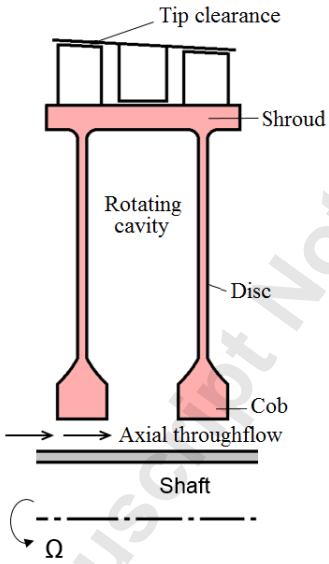


**Fig. 2: Simplified diagram of single compressor cavity**

Journal of Engineering for Gas Turbines and Power. Received June 07, 2017;
Accepted manuscript posted December 15, 2017. doi:10.1115/1.4038756


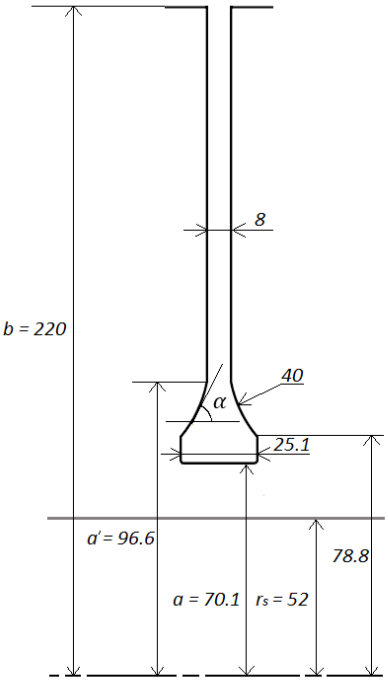


**Fig. 3: Simplified diagram of instrumented disc of Sussex rig (Dimensions in mm.)**

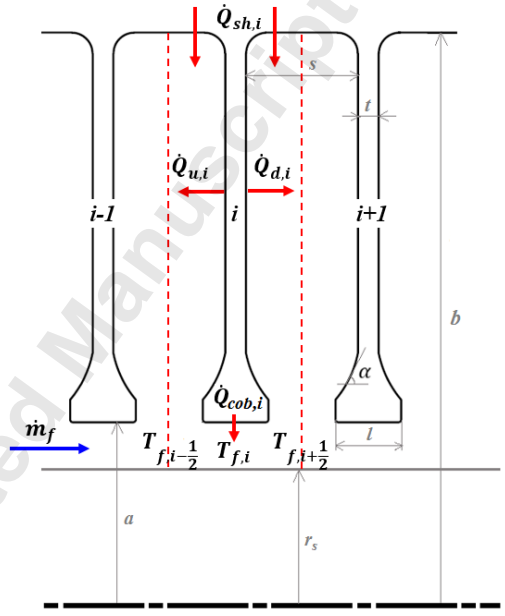


**Fig. 4: Control volume for temperature rise of axial throughflow**

Journal of Engineering for Gas Turbines and Power. Received June 07, 2017;
Accepted manuscript posted December 15, 2017. doi:10.1115/1.4038756


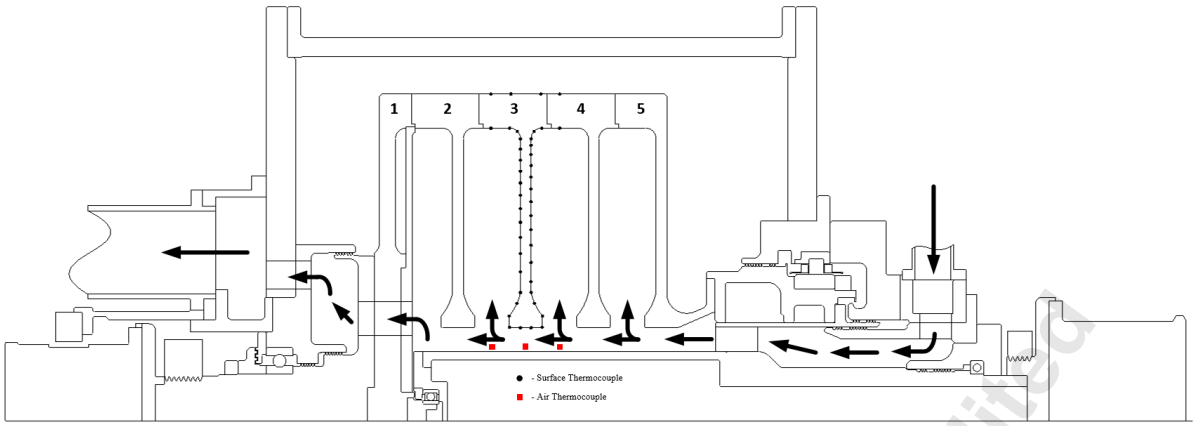


**Fig 5: Cross-section of Sussex Multiple-Cavity Rig**

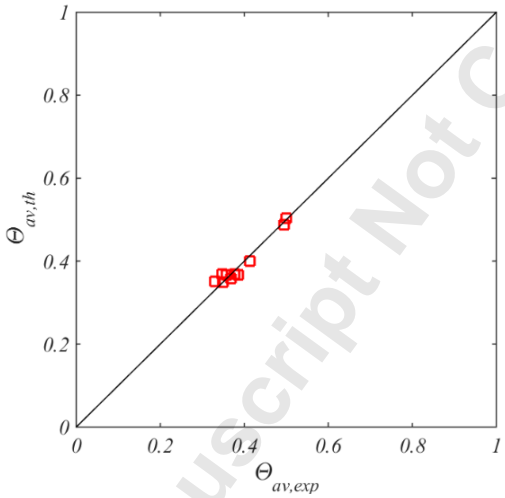


**Fig. 6: Comparison between theoretical and experimentally-derived average disc temperatures; symbols denote experimental values.**

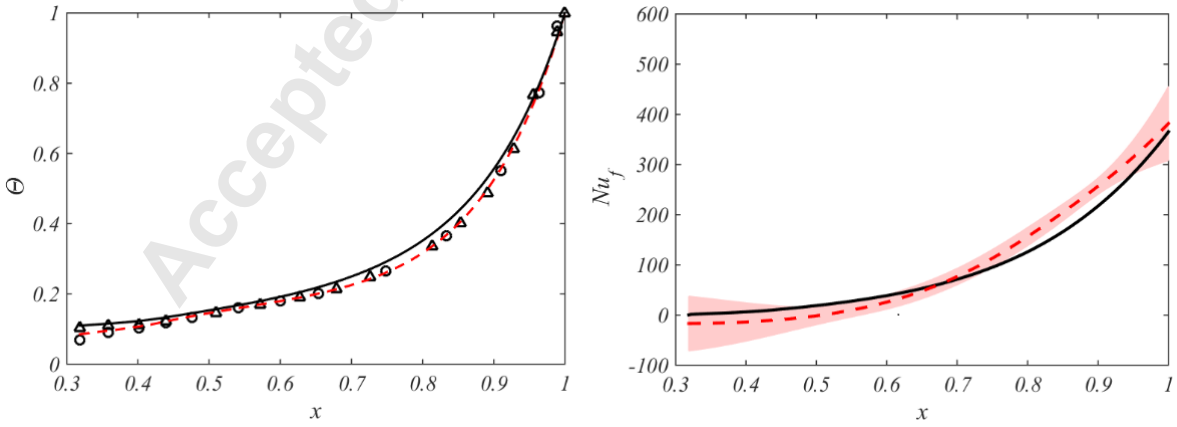


**Fig. 7: Distributions of nondimensional temperature and Nusselt numbers for Case a ($Ro \approx 0.6, Gr_f = 2.5 \times 10^{11}, Re_\phi = 1.6 \times 10^6, Re_z = 5.1 \times 10^4$). Solid lines are theoretical curves; broken lines are**

Journal of Engineering for Gas Turbines and Power. Received June 07, 2017;
Accepted manuscript posted December 15, 2017. doi:10.1115/1.4038756


**experimentally-derived curves; shading shows uncertainty in $Nu_f$; symbols denote temperature measurements.**

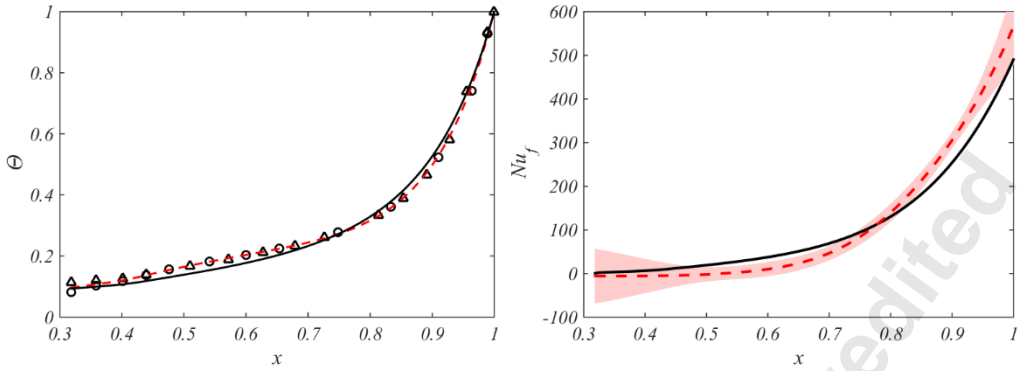


**Fig. 8 (a): Case b1($Gr_f = 1.0 \times 10^{12}, Re_\phi = 3.0 \times 10^6, Re_z = 5.0 \times 10^4$).**

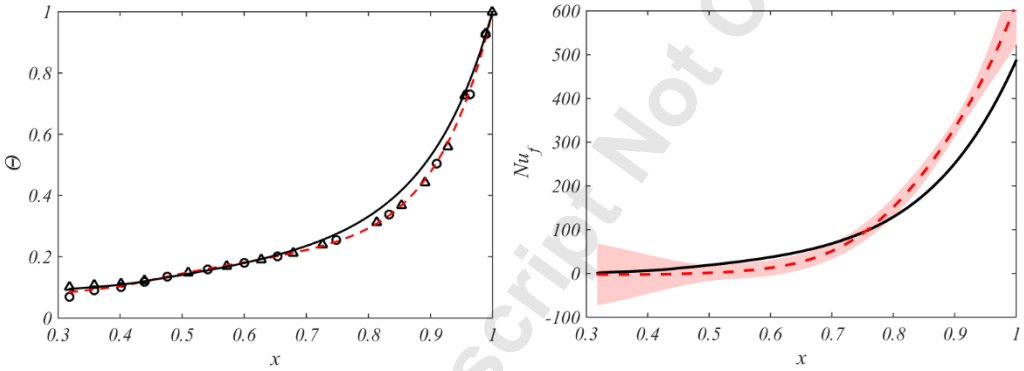


**Fig. 8 (b): Case b2($Gr_f = 1.0 \times 10^{12}, Re_\phi = 3.0 \times 10^6, Re_z = 5.0 \times 10^4$).**

**Fig. 8: Distributions of nondimensional temperature and Nusselt numbers for Case b ($Ro \approx 0.3$ ). Solid lines are theoretical curves; broken lines are experimentally-derived curves; shading shows uncertainty in $Nu_f$; symbols denote temperature measurements.**

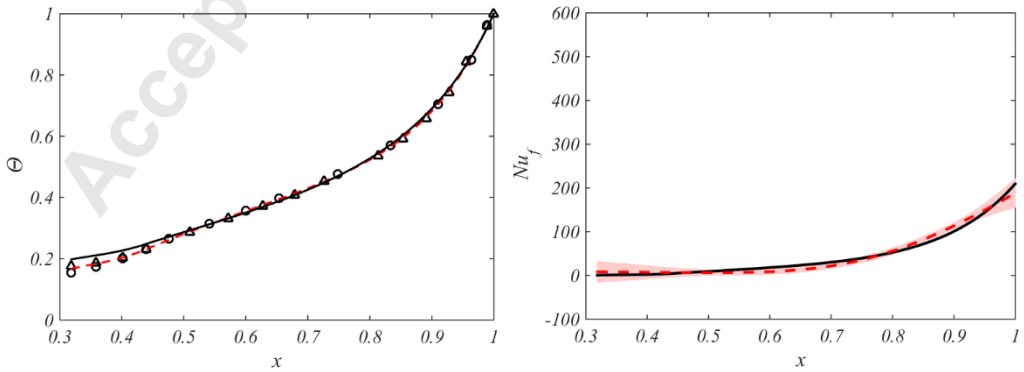


**Fig. 9 (a): Case c1 ($Gr_f = 4.2 \times 10^{11}, Re_\phi = 3.0 \times 10^6, Re_z = 2.5 \times 10^4$).**

Journal of Engineering for Gas Turbines and Power. Received June 07, 2017;
Accepted manuscript posted December 15, 2017. doi:10.1115/1.4038756


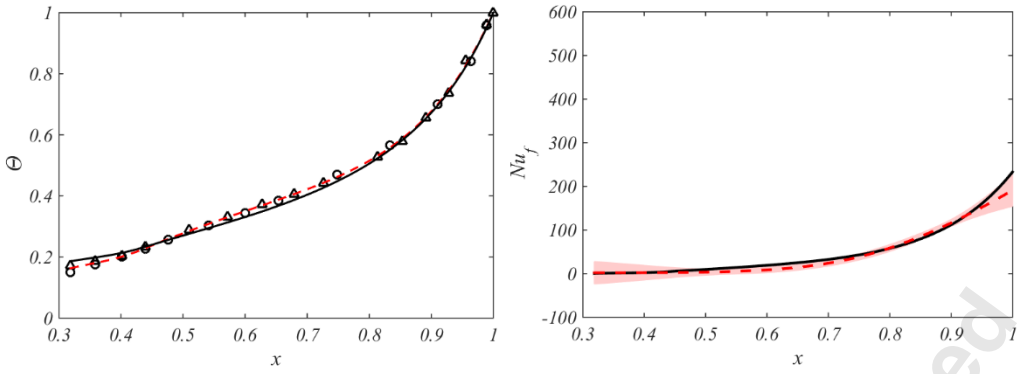


**Fig. 9 (b): Case c2 ($Gr_f = 4.5 \times 10^{11}, Re_\phi = 3.0 \times 10^6, Re_z = 2.5 \times 10^4$).**

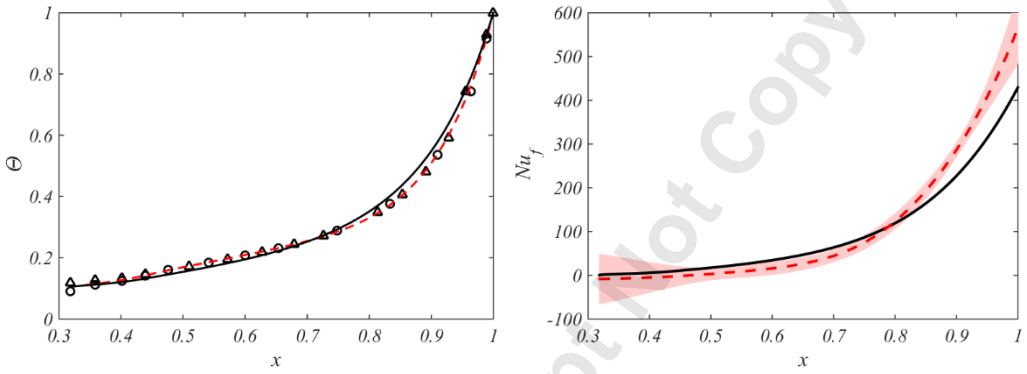


**Fig. 9 (c): Case c3 ($Gr_f = 6.8 \times 10^{11}, Re_\phi = 2.5 \times 10^6, Re_z = 2.4 \times 10^4$).**

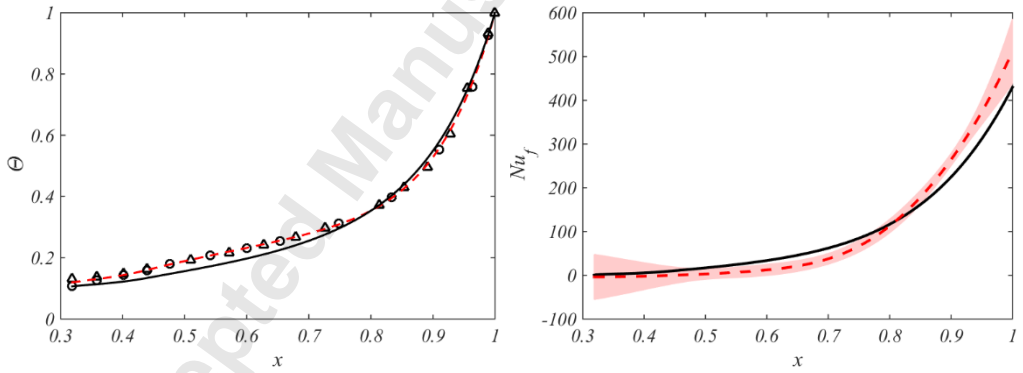


**Fig. 9 (d): Case c4 ($Gr_f = 7.2 \times 10^{11}, Re_\phi = 2.7 \times 10^6, Re_z = 2.4 \times 10^4$).**

Journal of Engineering for Gas Turbines and Power. Received June 07, 2017;
Accepted manuscript posted December 15, 2017. doi:10.1115/1.4038756


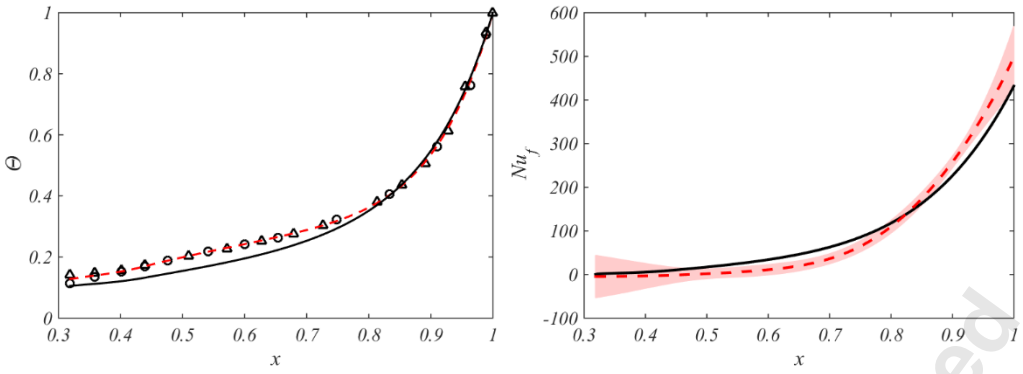


**Fig. 9 (e): Case c5 ($Gr_f = 7.2 \times 10^{11}, Re_\phi = 2.7 \times 10^6, Re_z = 2.4 \times 10^4$).**

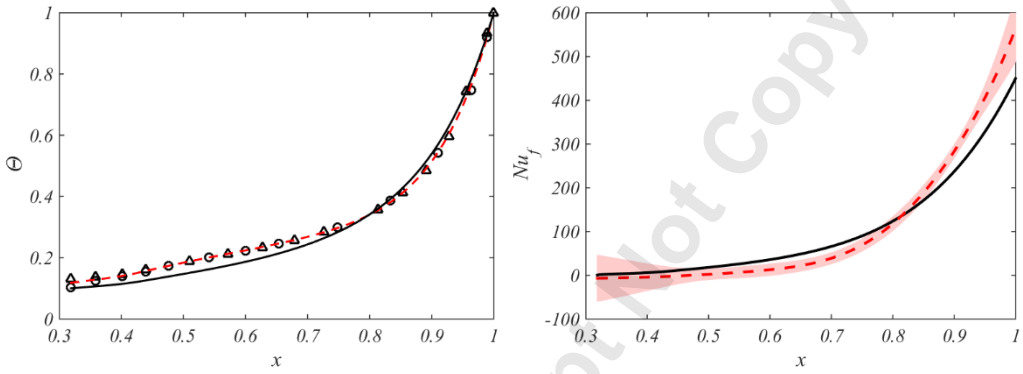


**Fig. 9 (f): Case c6 ($Gr_f = 7.8 \times 10^{11}, Re_\phi = 2.7 \times 10^6, Re_z = 2.5 \times 10^4$).**

**Fig. 9: Distributions of nondimensional temperature and Nusselt numbers for Case c ($Ro \approx 0.2$). Solid lines are theoretical curves; broken lines are experimentally-derived curves; shading shows uncertainty in $Nu_f$; symbols denote temperature measurements.**

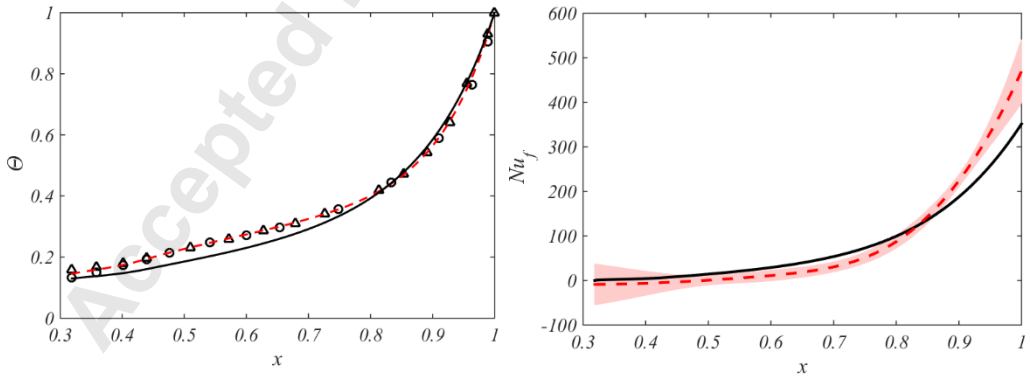


**Fig. 10: Distributions of nondimensional temperature and Nusselt numbers for Case d ($Ro \approx 0.2$, $Gr_f = 4.1 \times 10^{11}, Re_\phi = 2.1 \times 10^6, Re_z = 1.1 \times 10^4$). Solid lines are theoretical curves; broken lines are**

Journal of Engineering for Gas Turbines and Power. Received June 07, 2017;
Accepted manuscript posted December 15, 2017. doi:10.1115/1.4038756


**experimentally-derived curves; shading shows uncertainty in $Nu_f$; symbols denote temperature measurements.**

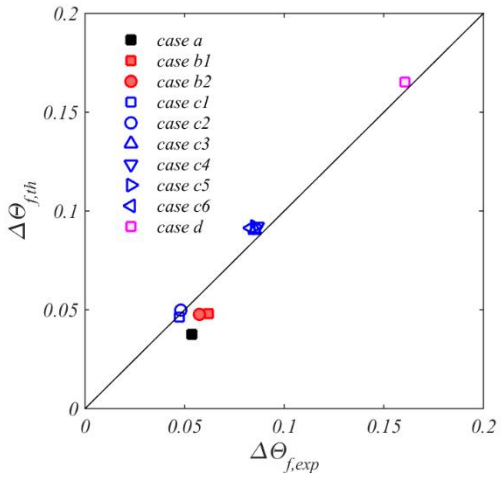


**Fig. 11: Comparison between modelled and experimental nondimensional temperature rise of axial throughflow.**